Supplementary Information (SI) for Energy & Environmental Science.

Microstructure of Electrodeposited Lithium and its Evolution During Cycling when Using Metal Interlayers in "Anode-Free" Solid-State Batteries

Juri Becker[1Δ], Luca Schuster[1Δ], Sascha Kremer[1], Till Fuchs[2] and Jürgen Janek[1*]*

[1]Institute of Physical Chemistry and Center for Materials Research (ZfM), Justus-Liebig-University Giessen, Heinrich-Buff-Ring 17, D-35392 Giessen, Germany.

[2]Institute of Experimental Physics I and Center for Materials Research (ZfM), Justus-Liebig-University Giessen, Heinrich-Buff-Ring 16, D-35392 Giessen, Germany.

Δ Equal contribution

Supporting Information

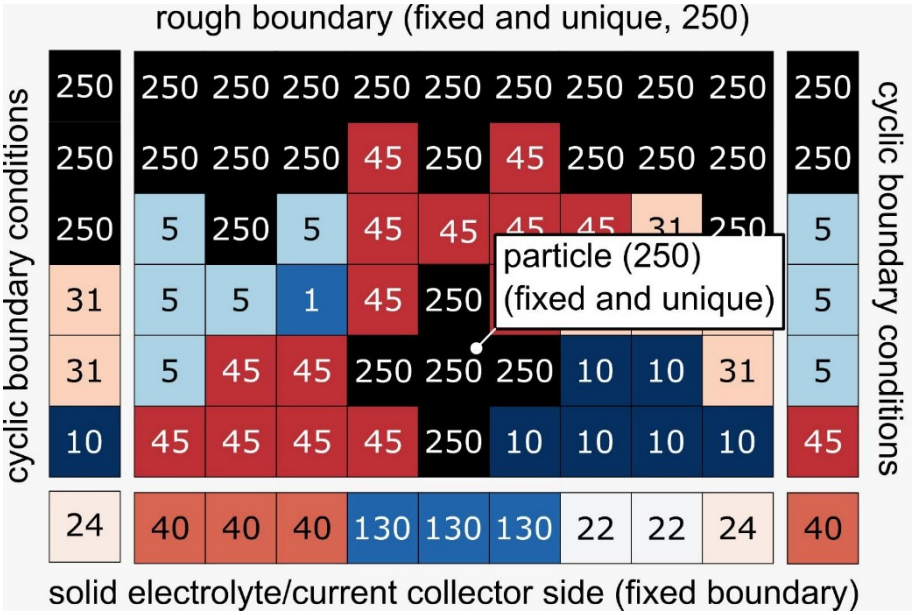

Figure S1: Scheme of the simulation approach and the cyclic boundary conditions for the Monte Carlo Potts model. The color and number within an MCU indicate the orientation of the respective MCU. The solid electrolyte on the bottom is simulated as a fixed boundary, i.e. its microstructure does not change throughout the simulation. Same is the case for the secondary particles introduced which are shown in black. Their orientation (250) is unique and fixed.

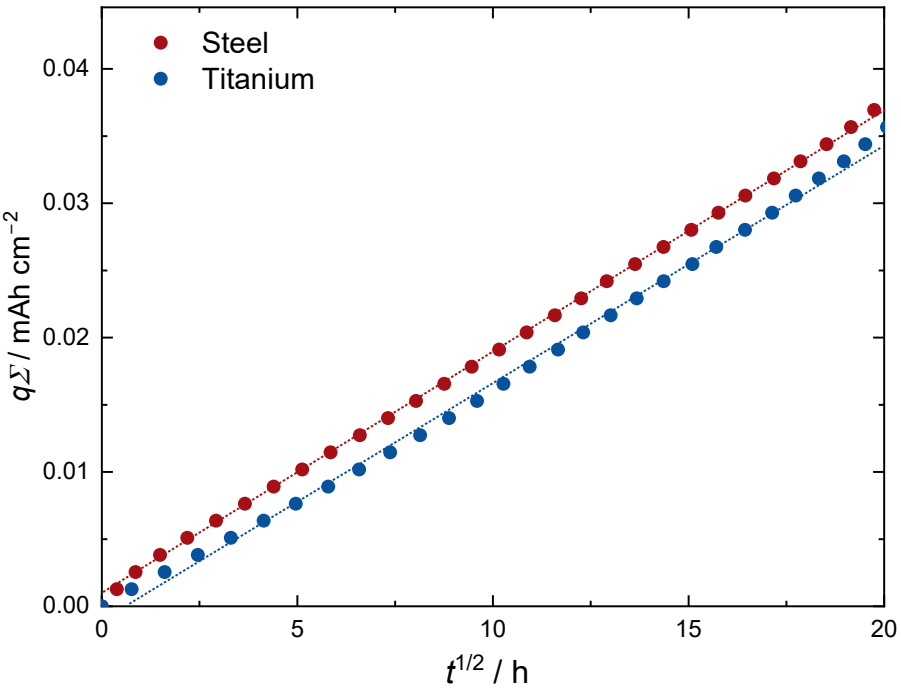

Figure S2. Results from coulometric titration time analysis (CTTA) performed on a steel and titanium current collector. The accumulated charge of lithium deposited on the WE is plotted against the square root of the overall elapsed time.

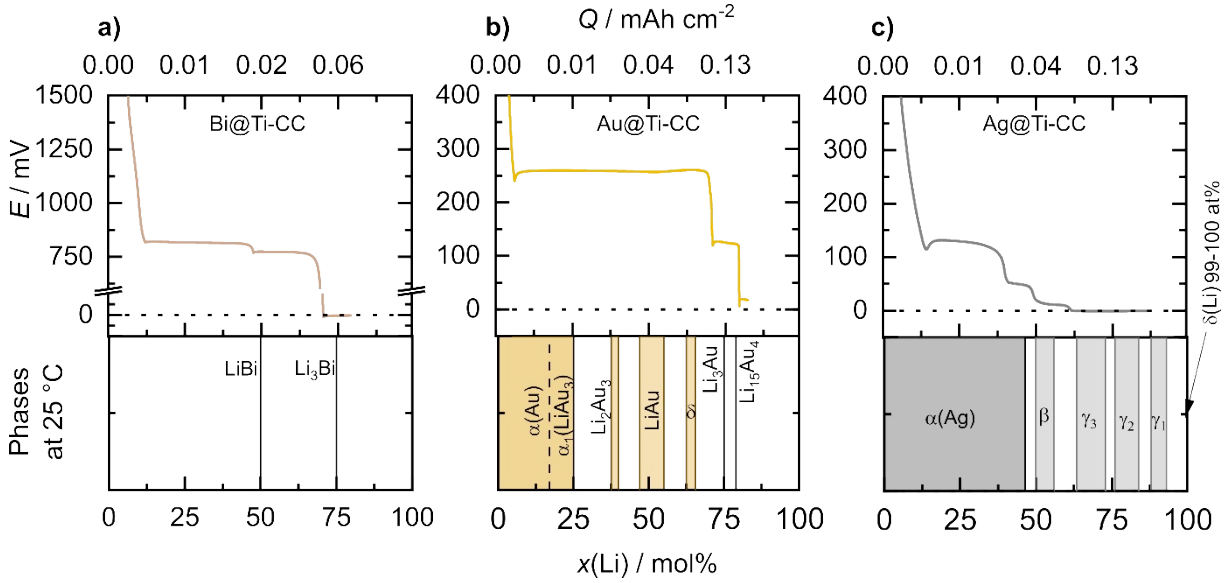

Figure S3. Voltage profiles during alloy formation on/with 160 nm of bismuth (a), gold (b), and silver (c) are shown, with an applied current density of 3 µA cm^{-2}. The voltage is plotted against the lithium molar fraction and accumulated charge. Below the profiles, the distinct alloy phases at 25 °C, taken from published phase diagrams[1–3], are displayed as a function of lithium molar fraction.

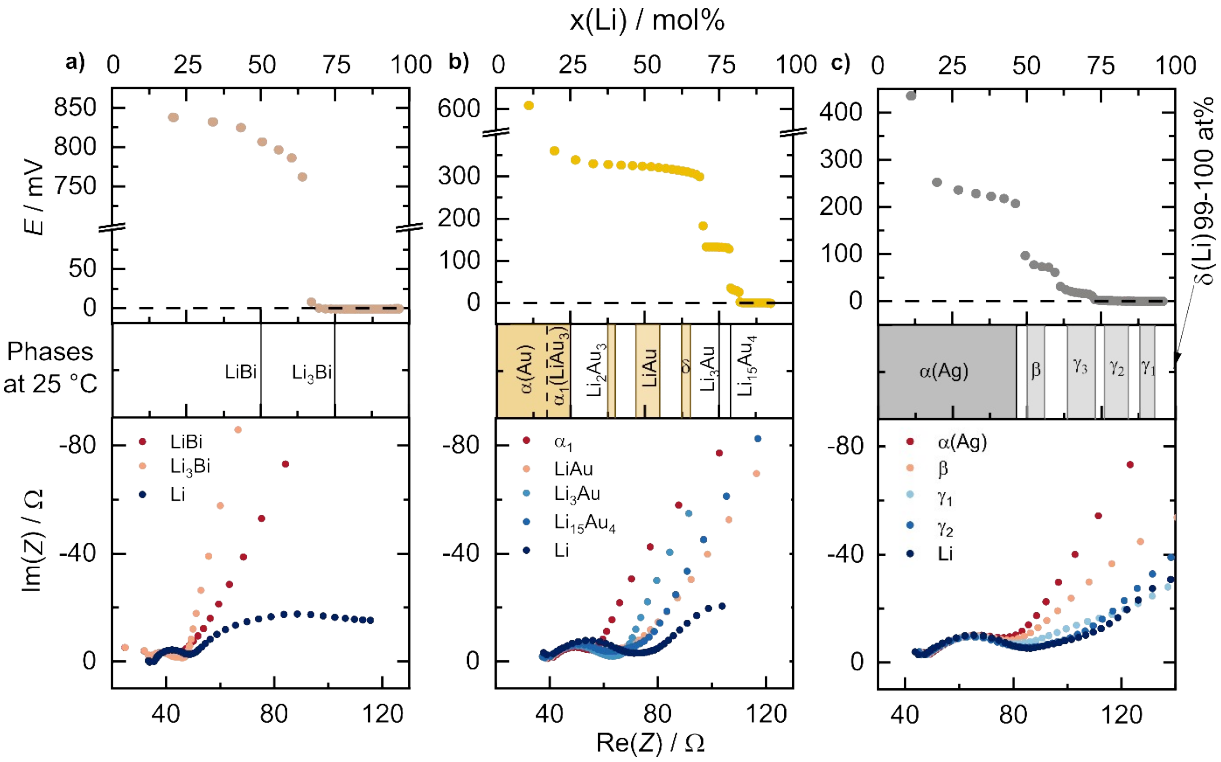

Figure S4: Electrochemical characterization of the alloying steps when plating lithium on a 160 nm thick bismuth interlayer (a), gold (b), and silver (c) using coulometric titration. On the top, the voltage during the resting period is shown at different stages of lithiation. Below the profiles, the distinct alloy phases, as taken from published phase diagrams[1–3], at 25 °C are displayed as a function of lithium molar fraction. At the bottom, electrochemical impedance spectra, acquired at times where the distinct alloy phases are present, are shown. For more information, we refer to **Supplementary Note 1**.

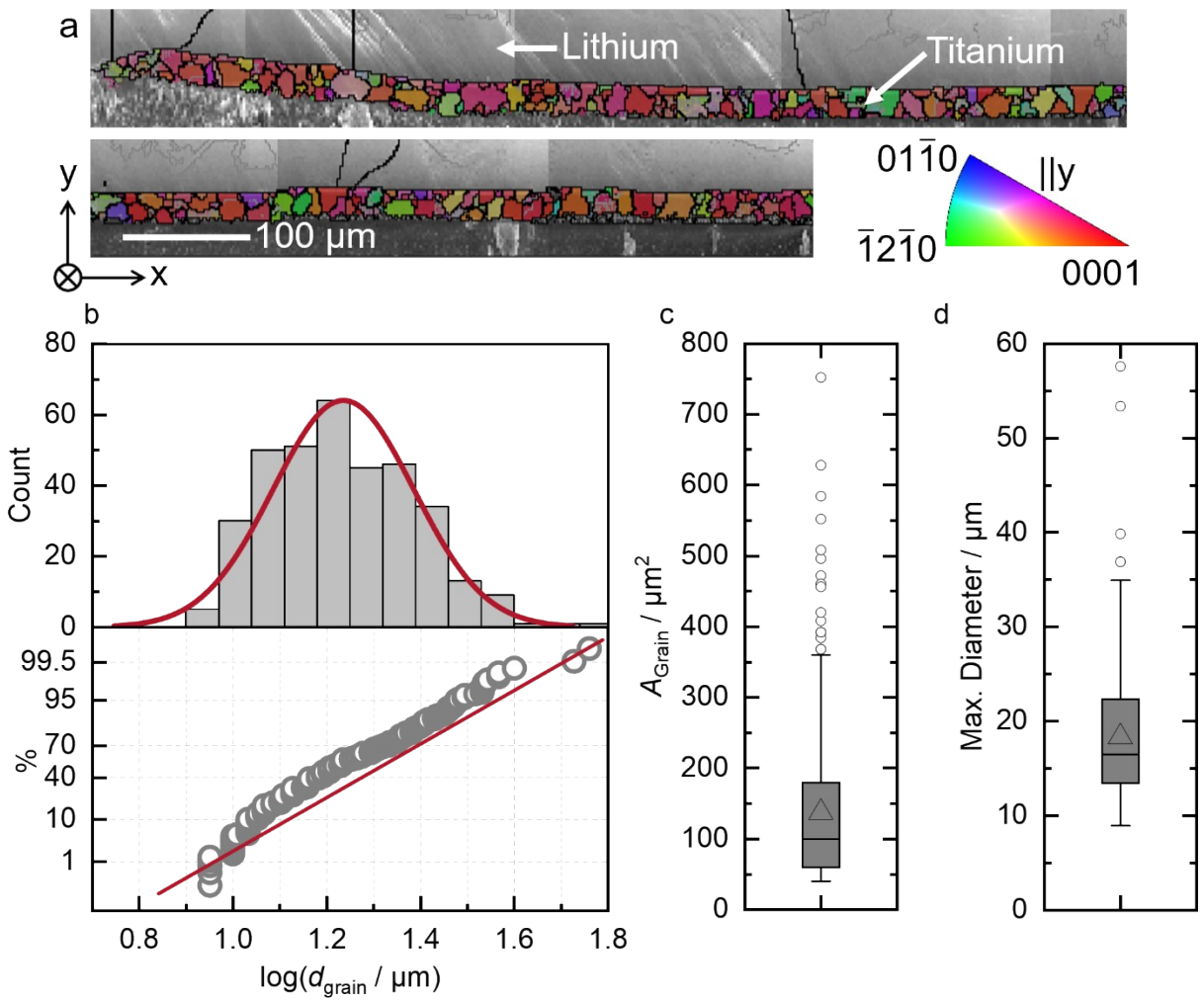

Figure S5: EBSD analysis of a cross-section of the titanium foil used in this study. (a) shows the inverse pole figure (IPF) map parallel to the y-direction. (b) presents the distribution of grain widths on a logarithmic scale. (c) and (d) display box plots of the grain areas and maximum grain diameters, respectively. Box plots of the grain surface areas and maximum grain diameters are shown in panels (c) and (d), respectively.

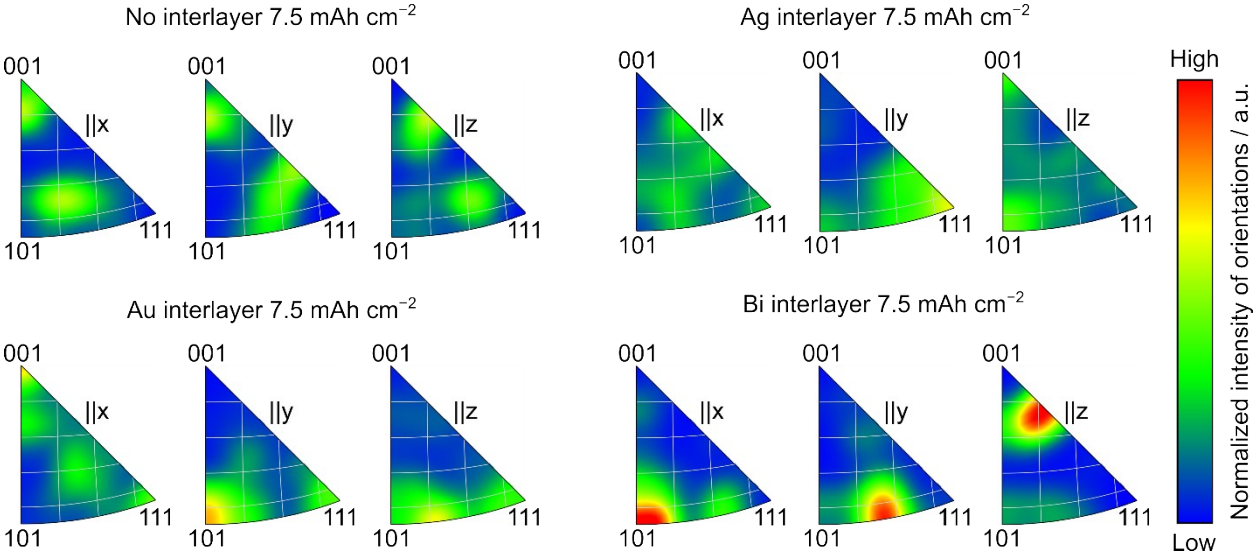

Figure S6. Inverse pole figures (IPFs) of the lithium layers electrodeposited at a current density of 150 µA cm^{-2} for 7.5 mAh cm^{-2} with and without interlayers. The orientations parallel to the *x*, *y* and *z*

directions are shown, as indicated above the IPFs. The normalized intensity of different orientations is shown according to the color scale bar on the right of the IPFs.

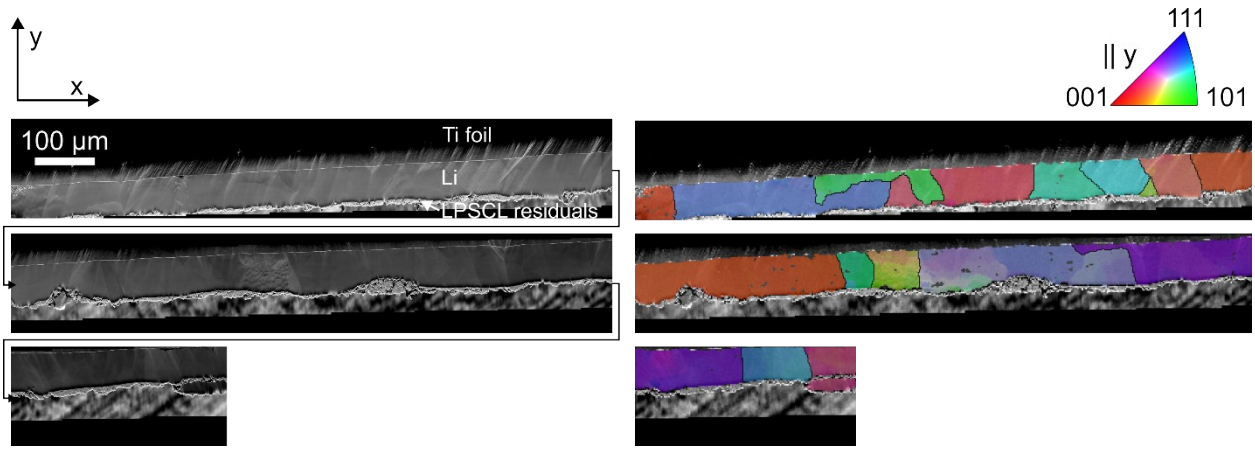

Figure S7. Full cross-section of a lithium layer electrodeposited at 150 µA cm^{-2} for 7.5 mAh cm^{-2} on a titanium foil without interlayer (related to Figure 1). The cross-section reveals a layered structure with the Ti foil at the top, lithium in the middle, and residual Li_6PS_5Cl particles at the bottom. Large-angle grain boundaries (> 10°) are marked with black lines. Due to the large width of the cross-section, it was divided into several small sections for illustration purposes. The “reading direction” is shown with arrows in the SEM image. The overlayed IPF maps for lithium on the right are given parallel to the *y*-direction. The scalebar represents 100 µm in all images.

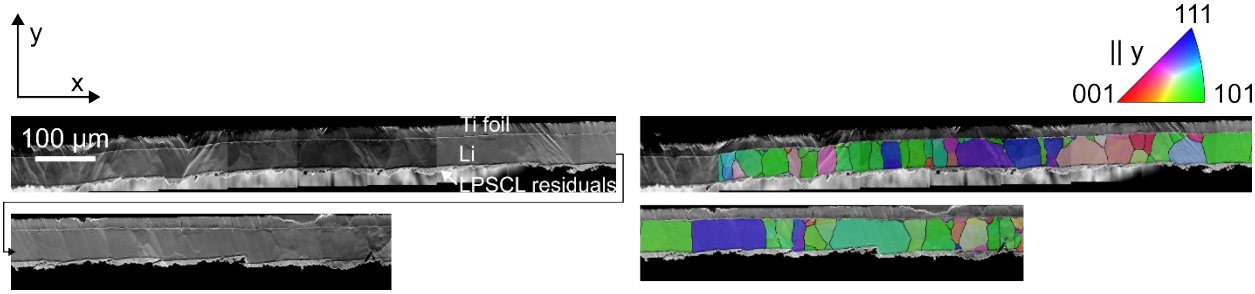

Figure S8. Full cross-section of a lithium layer electrodeposited at 150 µA cm^{-2} for 7.5 mAh cm^{-2} on a titanium foil with a gold interlayer (related to Figure 1). The cross-section reveals a layered structure with the Ti foil at the top, lithium in the middle, and residual Li_6PS_5Cl particles at the bottom. Large-angle grain boundaries (> 10°) are marked with black lines. Due to the large width of the cross-section, it was divided into two smaller sections for illustration purposes. The “reading direction” is shown with arrows in the SEM image. The overlayed IPF maps on the right for lithium are given parallel to the *y*-direction. The scalebar represents 100 µm in all images.

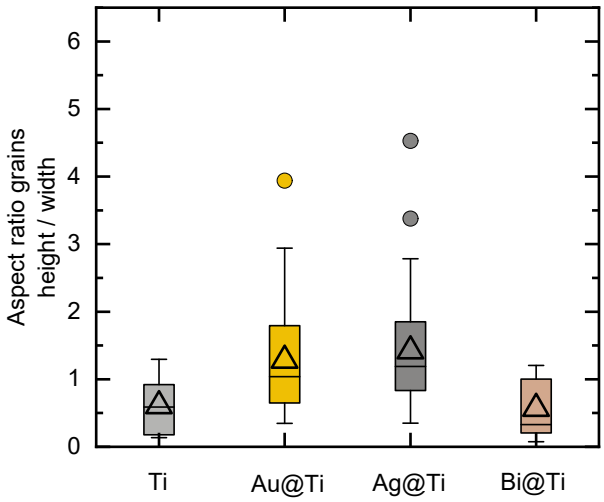

Figure S9. Aspect ratios (grain height divided by grain width) of the analyzed lithium grains electrodeposited with a current density of 150 µA cm^{-2} for 7.5 mAh cm^{-2} using different interlayer materials.

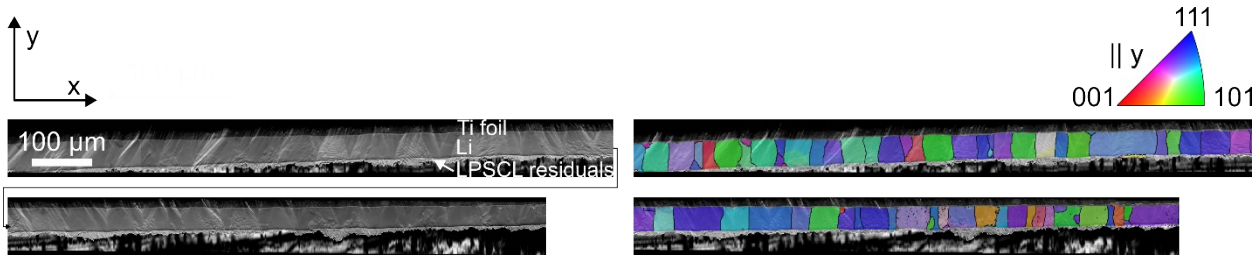

Figure S10. Full cross-section of a lithium layer electrodeposited at 150 µA cm^{-2} for 7.5 mAh cm^{-2} on a titanium foil with a silver interlayer (related to Figure 1). The cross-section reveals a layered structure with the Ti foil at the top, lithium in the middle, and residual Li_6PS_5Cl particles at the bottom. Large-angle grain boundaries (> 10°) are marked with black lines. Due to the large width of the cross-section, it was divided into two smaller sections for illustration purposes. The “reading direction” is shown with arrows in the SEM image. The overlayed IPF maps on the right for lithium are given parallel to the *y*-direction. The scalebar represents 100 µm in all images.

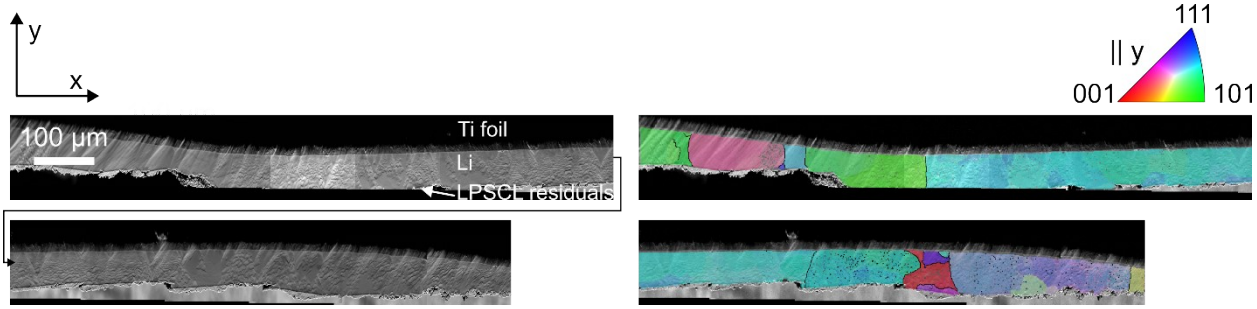

Figure S11. Full cross-section of a lithium layer electrodeposited at 150 µA cm^{-2} for 7.5 mAh cm^{-2} on a titanium foil with a bismuth interlayer (related to Figure 1). The cross-section reveals a layered structure with the Ti foil at the top, lithium in the middle, and residual Li_6PS_5Cl particles at the bottom. Large-angle grain boundaries (> 10°) are marked with black lines. Due to the large width of the cross-section, it was divided into two smaller sections for illustration purposes. The “reading direction” is shown with arrows in the SEM image. The overlayed IPF maps on the right for lithium are given parallel to the *y*-direction. The scalebar represents 100 µm in all images.

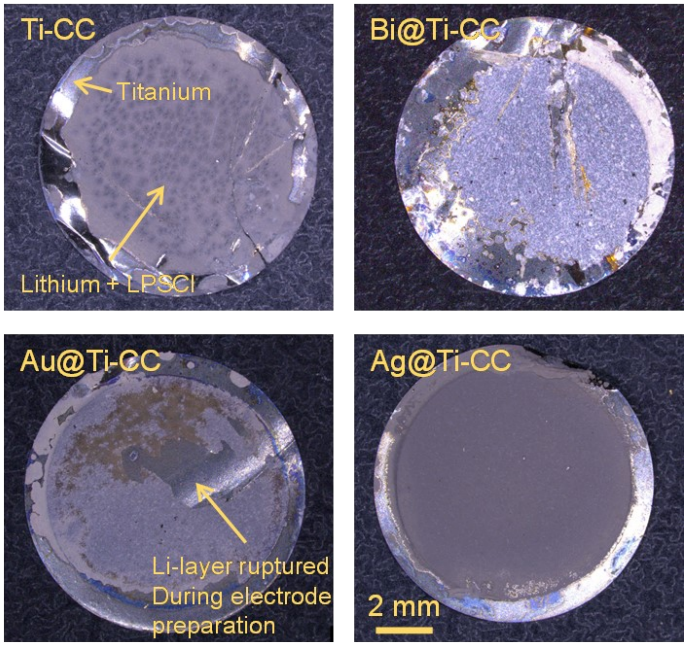

Figure S12. Optical images of the working electrodes after lithium electrodeposition and cell disassembly. The scalebar in the bottom right picture resembles 2 mm and is valid for all pictures. Please note that in the case of the pristine titanium foil, the whole electrode ($d \approx 10$ mm) was in contact with Li_6PS_5Cl. The diameter of the interlayers was only 8 mm.

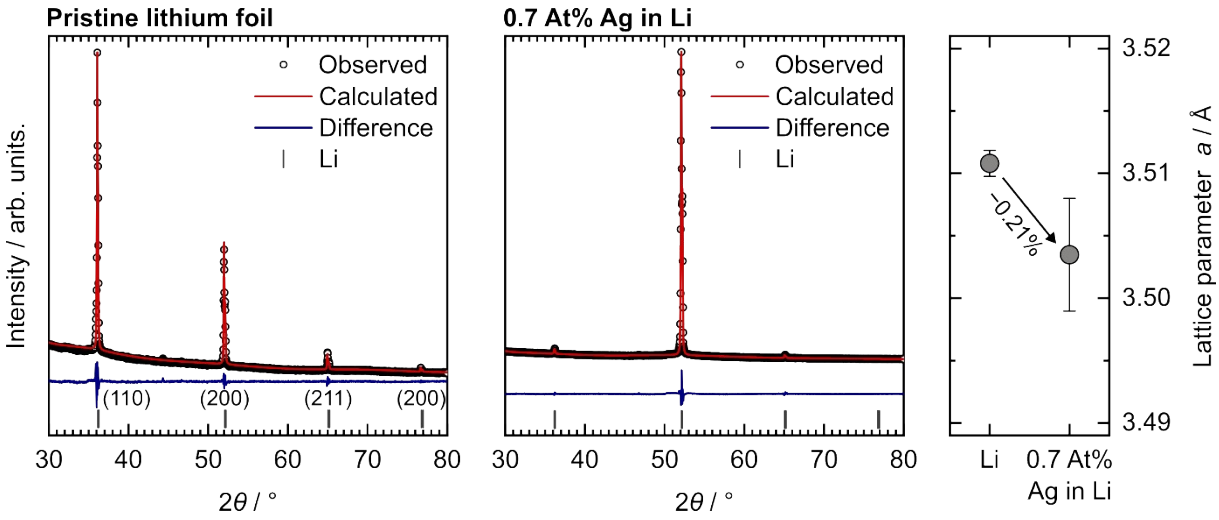

Figure S13: Comparison of X-Ray diffraction data acquired for pristine lithium foil (left plot) and a lithium foil with 0.7 At% dissolved Ag within (middle plot) with results of a Pawley-Fit. On the right, the extracted lattice parameter *a* shows a decrease with addition of Ag. For more information, we refer to **Supplementary Note 2**.

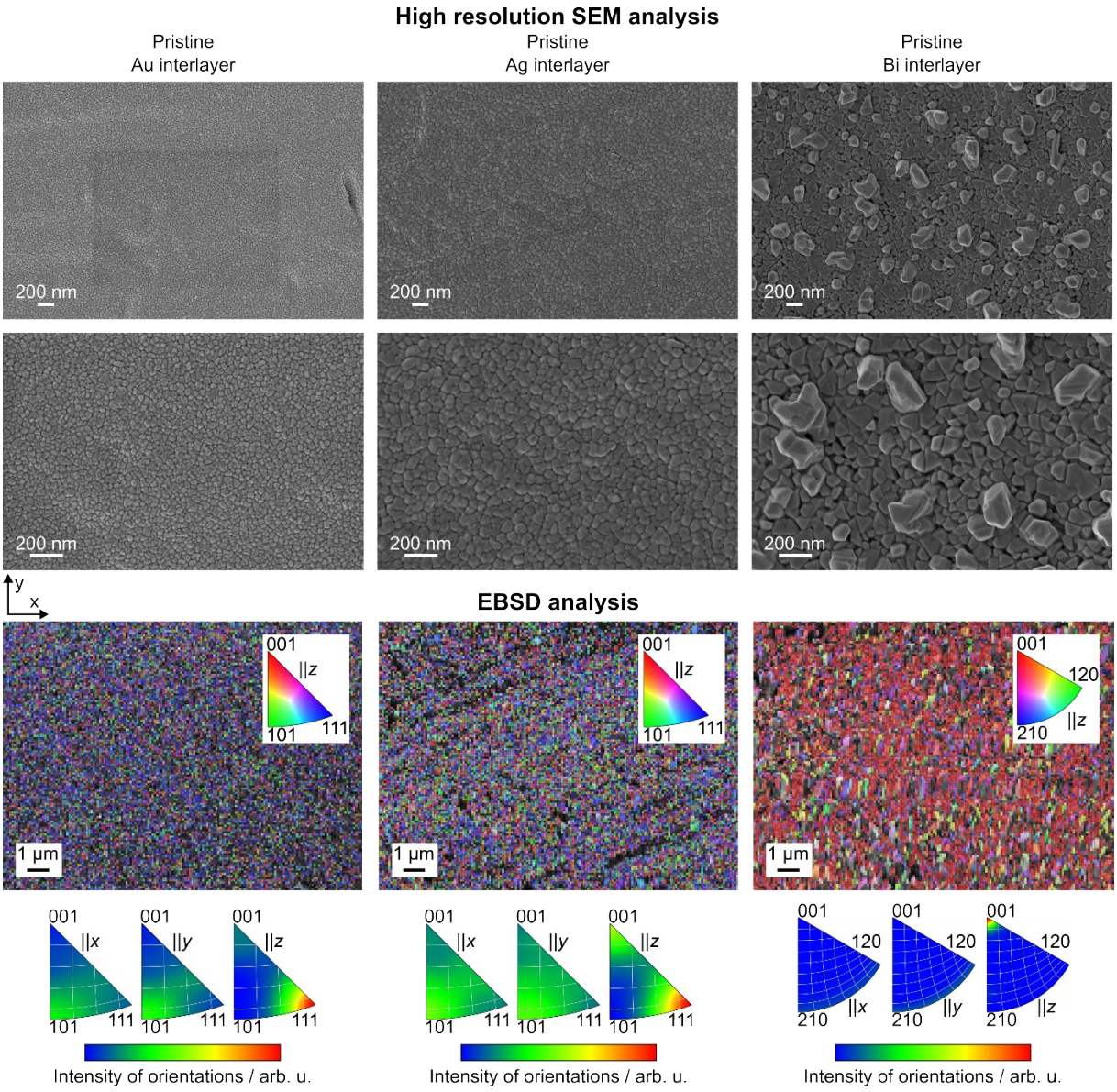

Figure S14: Microstructural analysis of the pristine interlayers. Columns correspond to the gold, silver, and bismuth interlayer, respectively. High-resolution SEM images are shown in the top row, while EBSD maps with the corresponding inverse pole figures are displayed below. Please note that the EBSD maps were acquired at different sample locations than the SEM images due to the distinct measurement geometries. Furthermore, the intensities of orientation were not normalized and cannot be compared in between different interlayer materials. More details are provided in **Supplementary Note 3**.

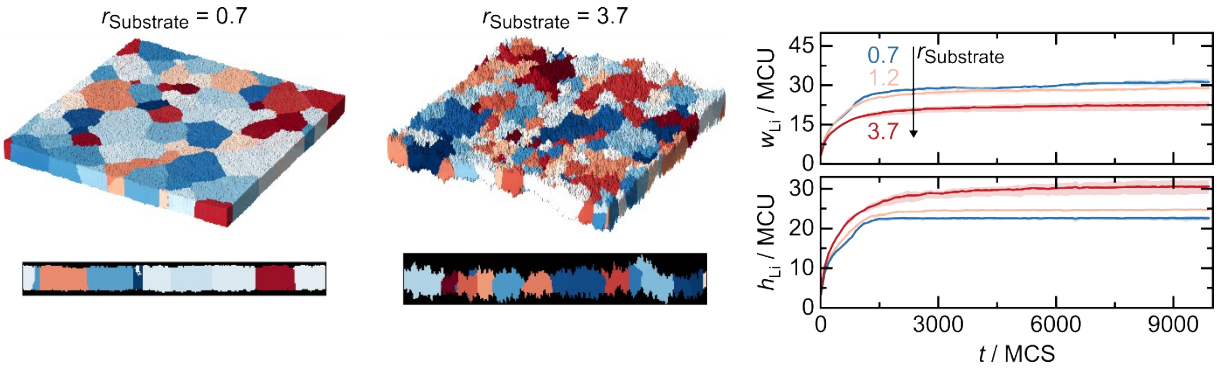

Figure S15: Simulation results of lithium microstructure evolution with different surface roughnesses of the substrate. The panel on the left shows two 3D microstructures with respective two 2D cross-sections

underneath. On the right, the evolution of the average grain width and height versus simulation time in Monte Carlo steps (MCS) is shown. For more information, we refer to **Supplementary Note 4**.

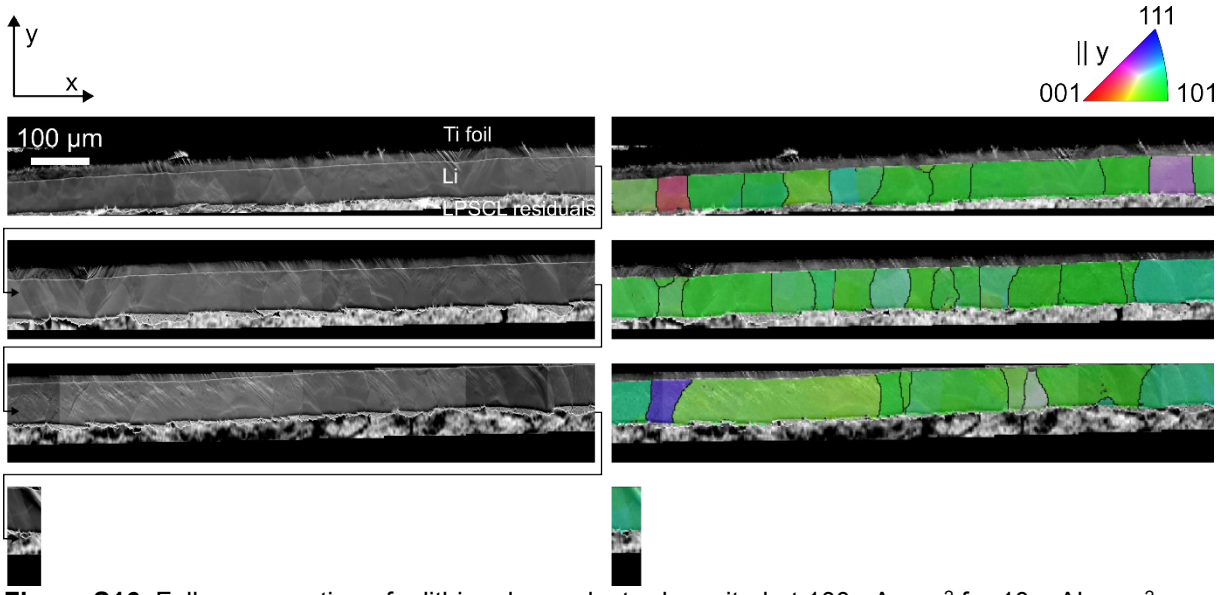

Figure S16. Full cross-section of a lithium layer electrodeposited at 100 µA cm^{-2} for 10 mAh cm^{-2} on a titanium foil with no interlayer (related to Figure 3) with subsequent stripping of 5 mAh cm^{-2} at the same current density. The cross-section reveals a layered structure with the Ti foil at the top, lithium in the middle, and residual Li_6PS_5Cl particles at the bottom. Large-angle grain boundaries (> 10°) are marked with black lines. Due to the large width of the cross-section, it was divided into several small sections for illustration purposes. The “reading direction” is shown with arrows in the SEM image. The overlayed IPF maps for lithium on the right are given parallel to the y-direction. The scalebar represents 100 µm in all images.

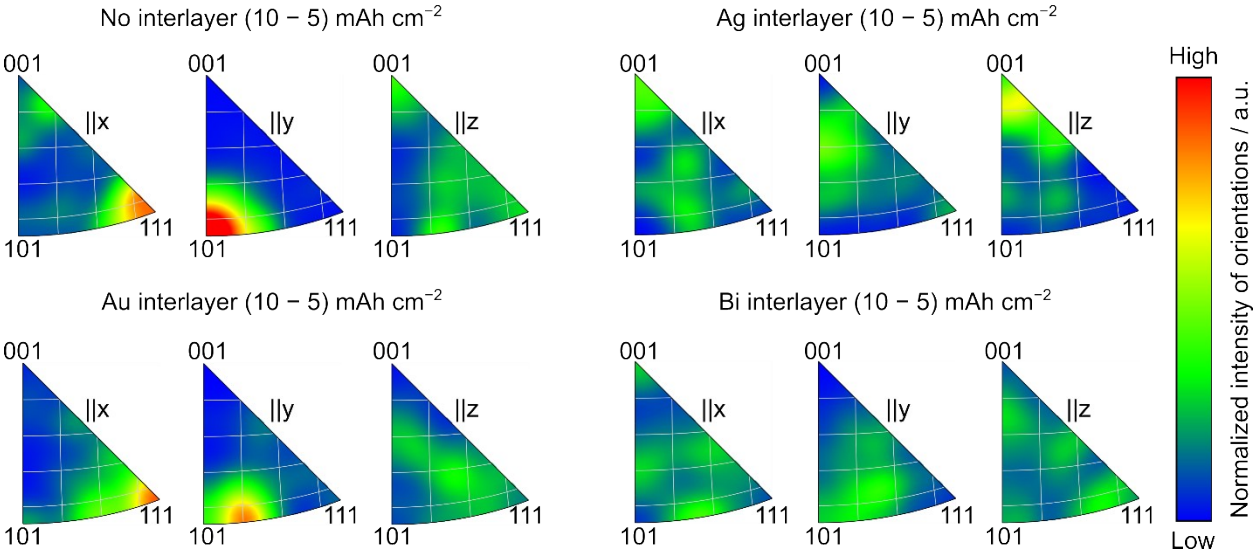

Figure S17. Inverse pole figures (IPFs) of the lithium layers electrodeposited on various substrates at a current density of 100 µA cm^{-2} for 10 mAh cm^{-2} and subsequent stripping of 5 mAh cm^{-2} using the same current density. The orientations parallel to the *x*, *y* and *z* directions are shown, as indicated above the IPFs. The normalized intensity of different orientations is shown according to the color scale bar on the right of the IPFs.

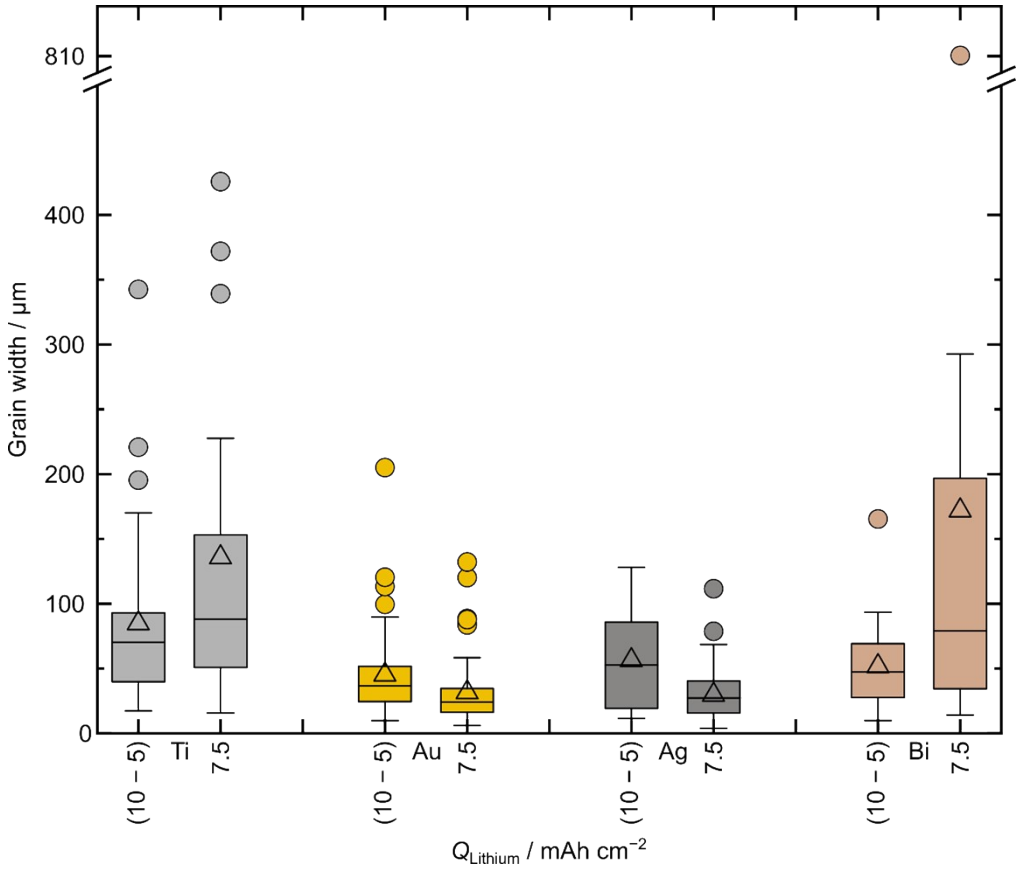

Figure S18: Grain widths of the lithium grains within the lithium layer with a total areal charge of 7.5 mAh cm^{-2} (after a plating step) or 5 mAh cm^{-2} (after a plating step followed by a stripping step). The samples denoted with (10 – 5) mAh cm^{-2} refer to the layers in which initially 10 mAh cm^{-2} of lithium were plated and subsequently 5 mAh cm^{-2} of these 10 mAh cm^{-2} were stripped again using a current density of 100 µA cm^{-2} (see Figure 3). The samples denoted with 7.5 mAh cm^{-2} refer to the layers in which solely a plating step was conducted for 7.5 mAh cm^{-2} of lithium at a current density of 150 µA cm^{-2} (see Figure 1). The used substrate for each case is given on the *x*-axis between the areal charges.

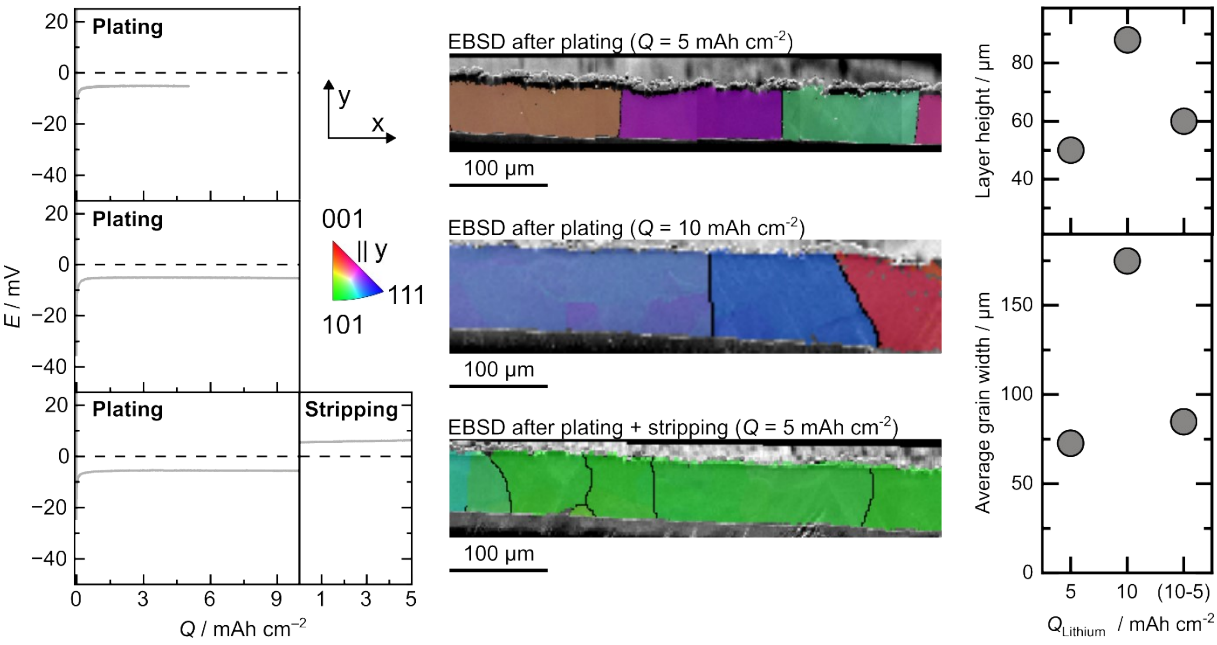

Figure S19: Grain size analysis of lithium deposited on pristine titanium foil. On the left, the voltage curves during lithium plating for samples with an areal charge of 5 mAh cm^{-2} and 10 mAh cm^{-2} are shown. For the sake of completeness, the voltage curve for plating and stripping of the

(10 − 5) mAh cm^{-2} sample from Figure 4 of the main text is also shown. In the middle, representative sections of large IPF maps for the three samples are shown. On the right, the extracted layer height and average grain width is shown. As evident from the average grain width plot, the average grain width for both samples with an absolute areal charge of 5 mAh cm^{-2} is comparable, despite their different cycling history.

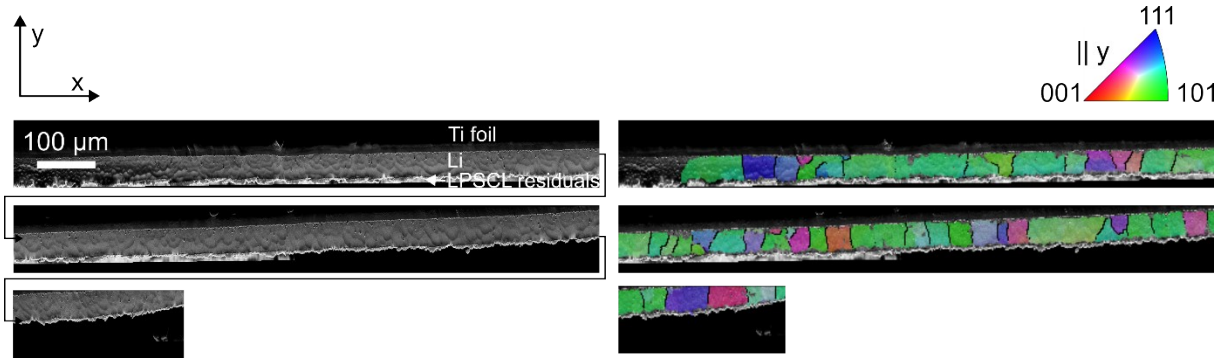

Figure S20. Full cross-section of a lithium layer electrodeposited at 100 µA cm^{-2} for 10 mAh cm^{-2} on a titanium foil with a gold interlayer (related to Figure 4) with subsequent stripping of 5 mAh cm^{-2}at the same current density. The cross-section reveals a layered structure with the Ti foil at the top, lithium in the middle, and residual Li_6PS_5Cl particles at the bottom. Large-angle grain boundaries (> 10°) are marked with black lines. Due to the large width of the cross-section, it was divided into three smaller sections for illustration purposes. The “reading direction” is shown with arrows in the SEM image. The overlayed IPF maps for lithium on the right are given parallel to the y-direction. The scalebar represents 100 µm in all images.

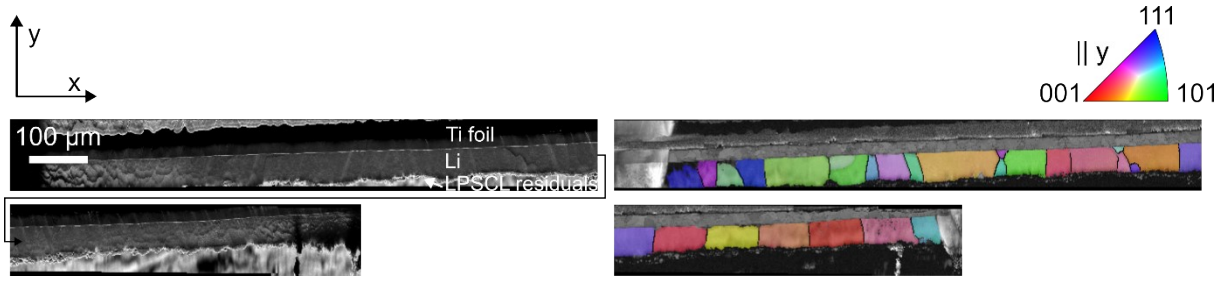

Figure S21. Full cross-section of a lithium layer electrodeposited at 100 µA cm^{-2} for 10 mAh cm^{-2} on a titanium foil with a silver interlayer (related to Figure 4) with subsequent stripping of 5 mAh cm^{-2} at the same current density. The cross-section reveals a layered structure with the Ti foil at the top, lithium in the middle, and residual Li_6PS_5Cl particles at the bottom. Large-angle grain boundaries (> 10°) are marked with black lines. Due to the large width of the cross-section, it was divided into two smaller sections for illustration purposes. The “reading direction” is shown with arrows in the SEM image. The overlayed IPF maps for lithium on the right are given parallel to the y-direction. The scalebar represents 100 µm in all images.

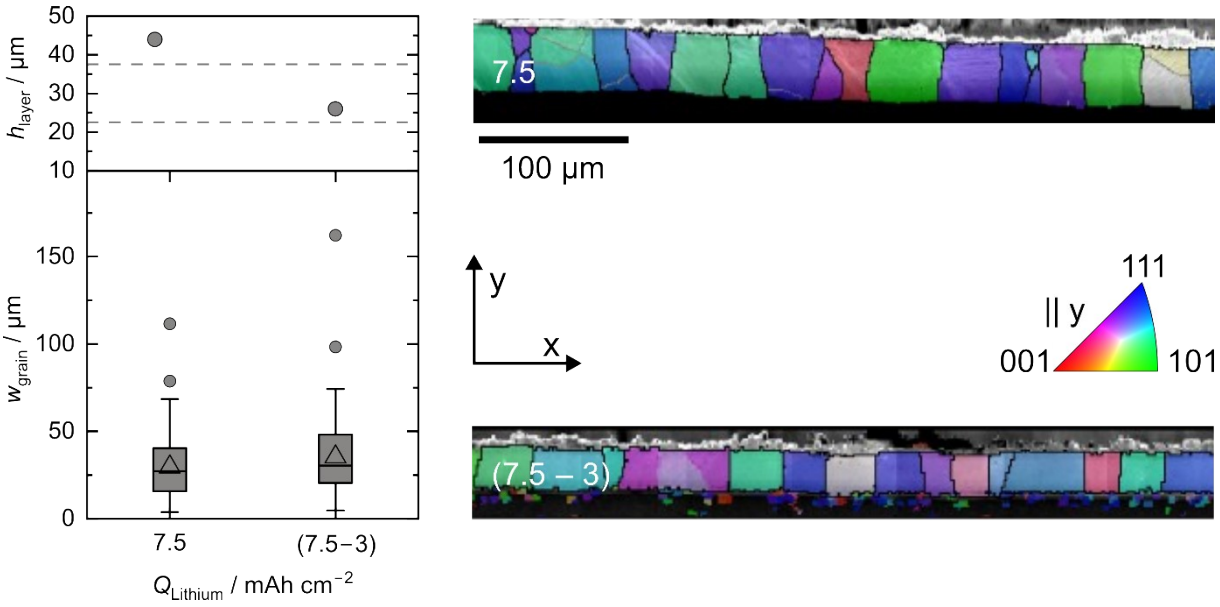

Figure 22: Grain size analysis of lithium deposited on titanium foil with a silver interlayer. The box plot on the left compares the layer thickness and grain size of a lithium layer plated on a silver interlayer for an areal charge of 7.5 mAh cm^{-2} and a lithium layer plated on a silver interlayer for an areal charge of 7.5 mAh cm^{-2} with subsequent partial stripping of 3 mAh cm^{-2}. Representative excerpts from larger IPF maps are shown on the right. Please note that the entire maps were analyzed to create the box plot.

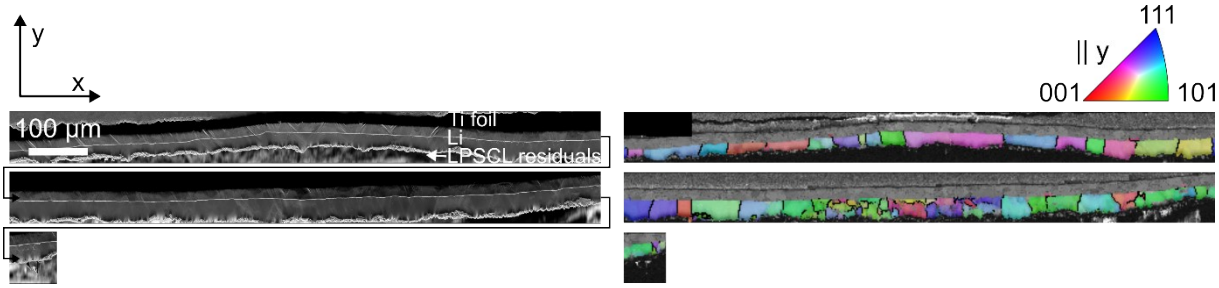

Figure S23. Full cross-section of a lithium layer electrodeposited at 100 µA cm^{-2} for 10 mAh cm^{-2} on a titanium foil with a bismuth interlayer (related to Figure 4) with subsequent stripping of 5 mAh cm^{-2} at the same current density. The cross-section reveals a layered structure with the Ti foil at the top, lithium in the middle, and residual Li_6PS_5Cl particles at the bottom. Large-angle grain boundaries (> 10°) are marked with black lines. Due to the large width of the cross-section, it was divided into two small sections for illustration purposes. The "reading direction" is shown with arrows in the SEM image. The overlayed IPF maps for lithium on the right are given parallel to the y-direction. The scalebar represents 100 µm in all images.

Supplementary Note 1 (Coulometric Titration)

To further analyze the potential evolution of distinct alloying phases, we conducted coulometric titration (CT) experiments. Here, an areal charge of 5 µAh cm^{-2} of lithium was incrementally deposited onto the negative electrode. Each deposition step was followed by a 15-minute relaxation period, during which the open-circuit voltage was recorded to capture its evolution with lithium concentration throughout the alloying process. After every relaxation step, potentiostatic electrochemical impedance spectroscopy was performed. Particular attention was given to changes in the low-frequency regime, as these may reflect differences in lithium transport behavior between coexisting or sequential alloy phases. The impedance spectra collected during lithium titration show distinct low-frequency behavior depending on the interlayer material. For bismuth, a pronounced increase in low-frequency impedance is observed as LiBi and Li_3Bi form, with the rise becoming steeper at higher lithium content. In the case of gold, the low-frequency slope evolves gradually with increasing lithiation, reflecting changes in the spectra as successive Au–Li alloy phases appear. For silver, the low-frequency region shows little variation once high lithium contents are reached, with spectra remaining nearly identical where the final alloy phases would be expected. These observations indicate material-dependent differences in the evolution of impedance during lithium titration across the three systems.

Supplementary Note 2 (Ag-Li alloys)

To measure the influence of dissolved silver on the lithium crystal structure, 0.0579 g silver was added to a stainless steel crucible containing a melt of 0.5126 g lithium resulting in a

composition of 0.7 At% silver and 99.3 At% lithium. The molten mixture was held at 260°C for three hours before cooling. After the mixture solidified and cooled to ambient temperature, it was transferred from the steel crucible to a glass jar. All steps were performed inside a glovebox under argon atmosphere. For the XRD measurement, a piece of the produced Li(Ag) solid solution was freed from passivation and pressed into foil form using a uniaxial press in the glove box. A spacer was used during pressing to ensure comparability of the sample heights. The sample thickness was approximately 350 µm in all cases. For the structural analysis of the produced foil, it was placed on a (911)-oriented silicon zero background holder and covered with Kapton polyimide foil inside the glove box to minimize reactions with the humidity outside the glove box. The sample was then transferred to an Empyrean powder diffractometer (PANalytical) with a copper K_α radiation source (λ_1 = 1.5405980 Å, λ_2 = 1.5444260 Å). The measurements were performed in a 2Θ range from 10° to 90° with a step size of 0.026°. The measurement time per angle step was 200 s. A Pawley fit was performed using Bruker's TOPAS-Academic V6 software to analyze the lattice parameters of the sample. The same procedure was repeated with pristine lithium samples, i.e., without dissolved silver. In this case, the lithium foils were pressed directly from the lithium rod and analyzed in the diffractometer. A total of three samples were analyzed for pristine and silver containing lithium. The mean value for the lattice parameter *a* was calculated from the three respective Pawley fits. Please note that during the fitting, the other lattice parameters *b* and *c* were set equal to *a* due to the cubic crystal structure.

Supplementary Note 3

To characterize the microstructure of the interlayers prior to lithium plating, SEM and EBSD analyses were performed on interlayers deposited on titanium foils (**Figure S14**). High-resolution SEM images were acquired at 2 kV and a working distance of 2 mm, while EBSD was conducted at 20 kV with a 70° sample tilt, a working distance of 12.5 mm, and a step size of 100 nm. All three interlayers are nanocrystalline with grain sizes (maximum Feret diameter) below 200 nm, following the order Au < Ag < Bi. With the chosen EBSD step size of 100 nm, most grains span only a single pixel, leading to a slight overestimation of the actual grain size. The acquired SEM images suggest that the actual grain sizes are even smaller. Interestingly, the inverse pole figures reveal a preferential orientation for all deposited interlayers, characterized by an alignment of the <111> direction parallel to the *z*-direction for Au and Ag, and the <001> direction for Bi. For the FCC metals (Au, Ag), this orientation corresponds to the most densely packed (111) lattice planes lying parallel to the substrate. This configuration

typically minimizes the surface free energy. Although the crystal structure of bismuth is more complex, the preferred orientation in the <001> direction suggests an analogous thermodynamic driving force, likely favoring the exposure of the stable, low-energy planes of its crystal structure during growth.

Supplementary Note 4

Figure S15 investigates the influence of substrate surface roughness on the resulting lithium microstructure**.** The 3D microstructures and corresponding 2D cross-sections on the left illustrate two cases with roughness values of 0.7 and 3.7. These values correspond to the arithmetic average of the profile height deviations from the mean line. The plot on the right shows the temporal evolution of average grain width and height for these surface roughnesses. An increased substrate roughness reduces the effective grain size, as grains grow more irregularly and fail to develop fully columnar structures. At a roughness of 3.7, the average grain height reaches a lower value than at 0.7, indicating that taller surface features act as pinning sites that restrict vertical growth. This pinning mechanism is similar to that caused by impurities and substrate microstructure. The surface asperities locally block curvature-driven growth, slowing both height and in-plane expansion of grains. Consequently, while grains continue to coarsen over time, the overall growth stagnates earlier compared to smoother surfaces, resulting in a finer and more constrained microstructure.

Supplementary Literature

(1) Sangster, J.; Pelton, A. D. The Bi-Li (Bismuth-Lithium) System. *Journal of Phase Equilibria* 1991, *12* (4), 447–450. https://doi.org/10.1007/BF02645966.

(2) Pelton, A. D. The Au−Li (Gold-Lithium) System. *Bulletin of Alloy Phase Diagrams* 1986, *7* (3), 228–231. https://doi.org/10.1007/BF02868994.

(3) Pelton, A. D. The Ag−Li (Silver-Lithium) System. *Bulletin of Alloy Phase Diagrams* 1986, *7* (3), 223–228. https://doi.org/10.1007/BF02868993.